RSC Advances

PAPER

View Article Online
View Journal | View Issue

Cite this: *RSC Adv.*, 2017, **7**, 10583

Homogeneous deposition of $Ni(OH)_2$ onto cellulose-derived carbon aerogels for low-cost energy storage electrodes†

Guoqing Zu,*[abc] Jun Shen,*[b] Zhihua Zhang,[b] Bin Zhou,[b] Xiaodong Wang,[b] Guangming Wu[b] and Yewen Zhang[c]

Received 9th November 2016
Accepted 28th December 2016

DOI: 10.1039/c6ra26566a

rsc.li/rsc-advances

Nano-architectured carbon aerogel/$Ni(OH)_2$ composites have been prepared *via* a wet chemical approach that combines the sol–gel preparation of a highly porous carbon aerogel using microcrystalline cellulose, a low-cost and renewable polymer, as the carbon source and subsequent homogeneous deposition of $Ni(OH)_2$ nanoparticles onto the backbone of the carbon aerogel *via* a two-step chemical precipitation process. The deposited $Ni(OH)_2$ has small particle size (3–10 nm) and uniform dispersion and is well exposed to the electrolyte. The resulting composite possesses an interconnected, three-dimensional, high-surface-area (327 m^2 g^{-1}) nanostructure, which provides efficient transport of electrolyte ions and electrons and enables a fuller utilization of $Ni(OH)_2$, thus leading to excellent electrochemical performance. The composite electrode exhibits high specific capacitance of 1906 and 1206 F g^{-1} at current density of 1 and 20 A g^{-1}, respectively, which are much higher than those of $Ni(OH)_2$. Moreover 89% capacitance is retained after 4000 cycles, implying a good cycling stability.

1. Introduction

Electrochemical energy storage devices have been widely studied in order to deal with the energy crisis. They are usually divided into two types, supercapacitors and batteries, in terms of their charge/discharge behaviors. Supercapacitors have drawn great interest as high-efficiency energy storage devices because of such advantages as long cycling life, high power density and short charging/discharging time.[1,2] However, the energy density of the supercapacitor is much lower than that of batteries, which limits its applications. The most widely studied electrode materials for energy storage devices are such transition metal oxides or hydroxides as RuO_2,[3] MnO_2,[4] Co_3O_4,[5] NiO[6] and $Ni(OH)_2$.[7] Among these transition metal oxides or hydroxides, $Ni(OH)_2$ is a promising candidate for high-performance energy storage electrodes due to its relatively low cost, natural abundance and high theoretical specific capacity.[7–9]

However, the reported $Ni(OH)_2$ usually exhibits poor cycling stability and low electric conductivity and its specific capacity is still far below the theoretical value.[10,11] This is probably because active $Ni(OH)_2$ is not effectively exposed to the electrolyte and the efficiency of the electrolyte ions and electron transport within the electrode material are relatively low, which limit the utilization of $Ni(OH)_2$ for capacity generation. There are mainly two methods for enhancing the electrochemical performance of $Ni(OH)_2$-based materials: the preparation of highly porous, high-surface-area $Ni(OH)_2$, and the growth of $Ni(OH)_2$ in a porous matrix of high electric conductivity such as activated carbon,[12–14] carbon nanotubes (CNTs),[8,15–18] graphene,[19–23] conductive polymers,[24] nickel foams,[2] and some other metals (Au, Ag, Cu, *etc.*).[25–27] The cycling stability of conductive polymers is usually unsatisfactory and the metals with excellent conductivities, such as Au and Ag, are expensive. Nickel foams are relatively low cost and can be directly used as binder-free electrodes. Among these matrixes, carbon-based matrixes demonstrate their advantage of high surface area, which enables more efficient charge and mass exchange, leading to high electrochemical performance. The interconnected, three-dimensional, conductive structure of the matrix, combined with the porous structure of $Ni(OH)_2$, facilitates electrolyte ions and electron transport and capacity generation from $Ni(OH)_2$ and effectively enhances the specific capacities and cycling stabilities. Recently, M. Xie *et al.* reported structurally stable $Ni(OH)_2$, grown *in situ* on nickel foam, for supercapacitors with high energy density of 57.9 W h kg^{-1}.[28] The electrodes obtained from $Ni(OH)_2$/ZnO and $Ni(OH)_2$/Cu composites grown on nickel foam exhibited a high energy density of 42 W h kg^{-1} and a high areal capacitance of 8.66 F cm^{-2}.[27,29] The $Ni(OH)_2$ electrodes

[a]*Tongji University, Shanghai, 200092, PR China. E-mail: guoqingzu@yahoo.com*
[b]*Shanghai Key Laboratory of Special Artificial Microstructure Materials and Technology, Pohl Institute of Solid State Physics, Tongji University, Shanghai, 200092, PR China. E-mail: shenjun67@tongji.edu.cn*
[c]*School of Electronics and Information Engineering, Tongji University, Shanghai, 200092, PR China*

† Electronic supplementary information (ESI) available: Photograph and SEM images of cellulose aerogel, N_2 adsorption/desorption isotherms for typical aerogels, CV curves of nanocellulose-derived CA, Nyquist curves for typical aerogels. See DOI: 10.1039/c6ra26566a

with carbon-based matrixes also showed excellent electrochemical capacitive performances. The reported $Ni(OH)_2$/graphene hydrogel electrodes exhibited a high specific capacitance of 1632 F g^{-1}.[30]

Carbon aerogel (CA) is another type of promising porous matrix for electrode materials because of its numerous advantages such as high porosity, high surface area, low density, excellent electrical conductivity, and open, three-dimensional, interconnected network.[31,32] Recently, several CA-based composites for energy storage electrodes have been reported, including CA/$NiCo_2O_4$ composite,[1] CA/Mn_3O_4 composite,[33] CA/Fe_3O_4 composite,[34] *etc.* The carbon sources of CAs are mainly organic aerogels that are usually prepared from such precursors as resorcinol/formaldehyde, cresol/formaldehyde, melamine/formaldehyde and resorcinol/pyrocatechol in an inert atmosphere.[35–38] Those traditional methods for the preparation of CAs involve harmful and expensive precursors and complex synthesis process, which limits the practical applications of CAs.[39,40] Recently, cellulose, a natural, renewable and abundant polymer, has attracted increasing attention as a source for the preparation of CAs.[41–43] Highly porous and high-surface-area CAs with high electric conductivities can be obtained from cellulose. It is reported that the electrochemical performance of the cellulose-derived CAs is comparable to that of the traditional CAs.[44,45]

In this study, high-surface-area CA/$Ni(OH)_2$ composites are prepared, for the first time, *via* a two-step chemical precipitation method using microcrystalline cellulose as the carbon source. First of all, cellulose aerogels are prepared by dissolving microcrystalline cellulose in an aqueous solution of NaOH, followed by gelation, regeneration and supercritical CO_2 drying. Subsequently, CAs are obtained by carbonizing the cellulose aerogels in an inert atmosphere. Finally, $Ni(OH)_2$ nanoparticles are homogeneously deposited onto the backbone of the high-surface-area CAs *via* a two-step chemical precipitation route. The precursor, namely nickel chloride, is first deposited onto the CA backbone, followed by the growth of $Ni(OH)_2$ nanoparticles on the backbone by introduction of water and an alkaline catalyst. This two-step chemical precipitation route ensures the deposition of $Ni(OH)_2$ nanoparticles on the backbone of the CA matrix and affords cellulose-derived CA/$Ni(OH)_2$ composites with high-surface-area, interconnected, three-dimensional and homogeneous nanostructures. This composite nanostructure enables $Ni(OH)_2$ to be well exposed to the electrolyte and provides efficient transport of electrolyte ions and electrons, leading to the excellent electrochemical performance of the CA/$Ni(OH)_2$ composites. The resulting composite materials may have application potentials in low-cost and high-performance energy storage devices.

2. Experimental

2.1 Materials

Ethanol (EtOH), methanol (MeOH), NaOH, KOH, aqueous ammonia (NH_3) (25–28 wt%), $NiCl_2 \cdot 6H_2O$ and microcrystalline cellulose were purchased from Sinopharm Chemical Reagent Corporation (China). Distilled water was purchased from the School of Environmental Science and Engineering of Tongji University. Polyvinylidene fluoride (PVDF) was purchased from Sigma-Aldrich, Co.

2.2 Synthesis of cellulose-derived CA

The synthesis procedure for the cellulose-derived CA is similar to that of our previous reports.[46] Distilled water was mixed with a certain amount of NaOH and microcrystalline cellulose at room temperature, separately. The temperatures of the mixtures of NaOH/H_2O (1 : 7 w/w) and cellulose/H_2O (1 : 7.5 w/w) were decreased to −10 °C and 5 °C, respectively, by putting them in a refrigerator. A transparent cellulose solution was obtained by mixing 24 g of NaOH/H_2O and 10.2 g of cellulose/H_2O with vigorous stirring for 30 min at room temperature. After the gel was formed, it was aged for 2 days, and then the wet gel was regenerated by immersing it in 120 mL of EtOH for 12 h. The regenerated wet gel was soaked 4 times in distilled water at 50 °C to remove the residual chemicals. Before drying, the wet gel was subjected to solvent exchange with ethanol 4 times to afford the alcogel. The cellulose aerogel was obtained after the alcogel was dried with supercritical CO_2 at 33 °C and 10 MPa. The cellulose aerogel was put into a tube furnace, followed by nitrogen flushing at a rate of 600 mL min^{-1} for 1 h. The temperature was then raised to 800 °C at a rate of 5 °C min^{-1} and kept at this temperature for 2 h under nitrogen flow at a rate of 300 mL min^{-1}. Finally, CA was obtained after the system was cooled to room temperature naturally.

2.3 Synthesis of cellulose-derived CA/$Ni(OH)_2$ composites

The CA/$Ni(OH)_2$ composite was prepared *via* a two-step chemical precipitation method according to the following procedure. The monolithic CA was first immersed in the mixture of methanol (5.0 mL) and $NiCl_2 \cdot 6H_2O$ (2.4 or 6.5 g) at 50 °C for 12 h, followed by drying at 50 °C for 1 day, for deposition of $NiCl_2$ on the CA backbone. Then, the dried CA composite was immersed in the mixture of methanol, aqueous ammonia and distilled water with the molar ratio of MeOH : NH_3 : H_2O being 10.5 : 1 : 3.5 at room temperature for 1 day for the formation of $Ni(OH)_2$ nanoparticles on the CA backbone. The CA/$Ni(OH)_2$ composite was obtained after washing with water and methanol and drying at 100 °C for 1 day. The content of $Ni(OH)_2$ in the composites deposited by 2.4 and 6.5 g $NiCl_2 \cdot 6H_2O$ was around 30 and 75 wt%, respectively, which was determined by the weight changes before and after the incorporation of $Ni(OH)_2$. The CA/$Ni(OH)_2$ composites with 30 and 75 wt% $Ni(OH)_2$ were denoted as CA/$Ni(OH)_2$/0.30 and CA/$Ni(OH)_2$/0.75, respectively.

For comparison, pure $Ni(OH)_2$ was also prepared according to the following two steps. First, $NiCl_2 \cdot 6H_2O$ (2 g) was dissolved in methanol (12 mL) at room temperature. Then, aqueous ammonia and distilled water (the molar ratio of MeOH : NH_3 : H_2O was 10.5 : 1 : 3.5) were added to the precursor solution with stirring for 30 min at room temperature. Pure $Ni(OH)_2$ was obtained after aging for 1 day, filtering, washing with water and methanol, and drying at 100 °C for 1 day.

2.4 Characterization

The morphologies of the samples were measured using a transmission electron microscope (TEM, JEOL-1230, JEOL, Japan) and a scanning electron microscope (SEM, XL30FEG, Philips, Netherlands). The compositions and crystallite structures were determined by powder X-ray diffraction (XRD) in a Rigata/max-C diffractometer using the Cu-Kα radiation (DX-2700, HaoYuan Instruments, China). The surface states of the samples were characterized by an X-ray photoelectron spectrometer (XPS, PHI-5000C ESCA, Perkin Elmer, USA) and a Raman spectrometer with 514.5 nm wavelength incident laser light (LabRAM HR800, HORIBA JOBIN YVON, France). The surface functional groups were investigated by Fourier transform infrared (FTIR) spectroscopy (TENSOR27, Bruker, Germany). The pore structure and SSA were measured by a N_2 adsorption analyzer (TriStar 3000, Quantachrome Instruments, USA). The SSA was determined using the (Brunauer–Emmett–Teller) BET method. The pore volume was calculated from the amount of N_2 adsorbed at a relative pressure of $P/P_0 = 0.99$. The pore size distribution and mean pore diameter were obtained from the adsorption branch of the isotherm *via* the Barrett–Joyner–Halenda (BJH) method.

2.5 Electrochemical measurement

The electrochemical measurements were carried out using an electrochemical working station (CHI660A, Shanghai, China) in a three-electrode system with a 6 M KOH solution as the electrolyte. The working electrode was prepared by loading the mixture of the active materials (carbon aerogel plus $Ni(OH)_2$), poly(vinylidene fluoride) (PVDF) and carbon black with a mass ratio of 8 : 1 : 1 on a graphite substrate, followed by drying at 80 °C for 12 h. The working area of the electrode was 1×1 cm^2 and the amount of the active materials was about 2 mg. A saturated calomel electrode (SCE) and Pt electrode served as the reference and counter electrodes, respectively. The cyclic voltammetry (CV) curves were measured within a potential range from −0.1 to 0.45 V and −0.3 to 0.6 V by varying the scan rate from 5 to 100 mV s^{-1} and 100 to 500 mV s^{-1}, respectively. Galvanostatic charge/discharge measurements were conducted within a potential window of −0.1 to 0.4 V with a constant current density of 1–20 A g^{-1}. The specific capacitance was calculated from the galvanostatic charge/discharge curve according to equation $Q = (I \times \Delta t)/(m \times \Delta V)$ where C is the specific capacitance (F g^{-1}), I is the discharge current (A), Δt is the discharge time (s), ΔV is the discharge voltage, and m is the active material mass of the electrode (g).

3. Results and discussion

3.1 Synthesis

Fig. 1 illustrates the fabrication process of the cellulose-derived CA/$Ni(OH)_2$ composite. The cellulose microcrystalline powders (as shown in Fig. 2a) were first converted into a monolithic cellulose aerogel by a sol–gel process, followed by supercritical CO_2 drying. Subsequently, the cellulose aerogel was carbonized in an inert atmosphere to afford monolithic cellulose-derived CA (Fig. 2b) as a nanoporous matrix. Finally, the cellulose-derived CA/$Ni(OH)_2$ composite was obtained after a two-step chemical precipitation process. In the first step of the chemical precipitation process, the precursor was deposited into the porous CA matrix by immersing the CA in the precursor solution ($NiCl_2 \cdot 6H_2O$/MeOH), followed by ambient drying. In the second step, the precursor was precipitated and $Ni(OH)_2$ nanoparticles were deposited onto the CA backbone by immersing the CA in the alkaline solution (NH_3/MeOH/H_2O), followed by solvent exchange and ambient drying. This fabrication method enabled the active material, namely $Ni(OH)_2$, to be deposited onto the backbone of the conductive nanoporous CA matrix obtained from a low-cost and renewable polymer, which is presumed to lower the cost and enhance the efficiency of capacity generation of $Ni(OH)_2$.

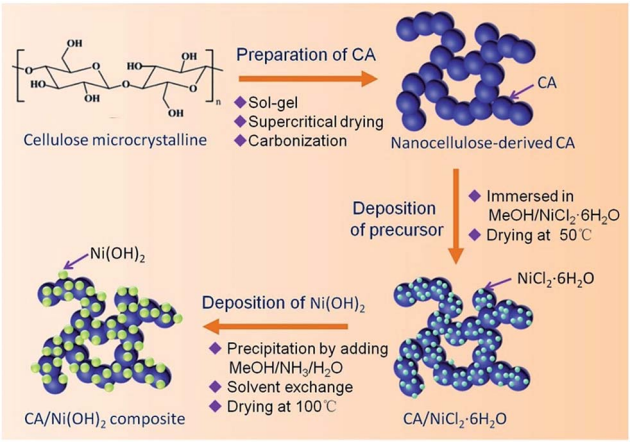

Fig. 1 Schematic of the fabrication process of the cellulose-derived CA/$Ni(OH)_2$ composite.

3.2 Morphology and appearance

As shown in Fig. S1,† the obtained cellulose aerogel is monolithic and exhibits randomly interconnected three-dimensional networks made up of fibrous nanoparticles with thickness of 40–60 nm. The SEM image (Fig. 2d) confirms that the cellulose-derived CA preserves the interconnected networks of the cellulose aerogel. Fig. 2e and f show the TEM images of the cellulose-derived CA. It can be seen that the CA exhibits randomly interconnected networks made up of fibrous particles with thicknesses in the range of 15–40 nm, which are smaller than that of the cellulose aerogel. The interconnected networks create abundant pores varying in size from several nanometers to around 100 nm, which confirms the nanoporous structure of the cellulose-derived CA. For comparison, pure $Ni(OH)_2$ (Fig. 2c) was also prepared *via* a similar chemical precipitation method. As shown in the SEM image (Fig. 2g) and TEM image at low magnification (Fig. 2h), the obtained $Ni(OH)_2$ exhibits randomly interconnected networks with numerous irregular aggregates larger than 100 nm. The TEM image at high magnification (Fig. 2i) shows that the aggregate is porous and made up of nanoparticles smaller than 20 nm. The corresponding selected area electron diffraction pattern (the inset of Fig. 2h) shows a set

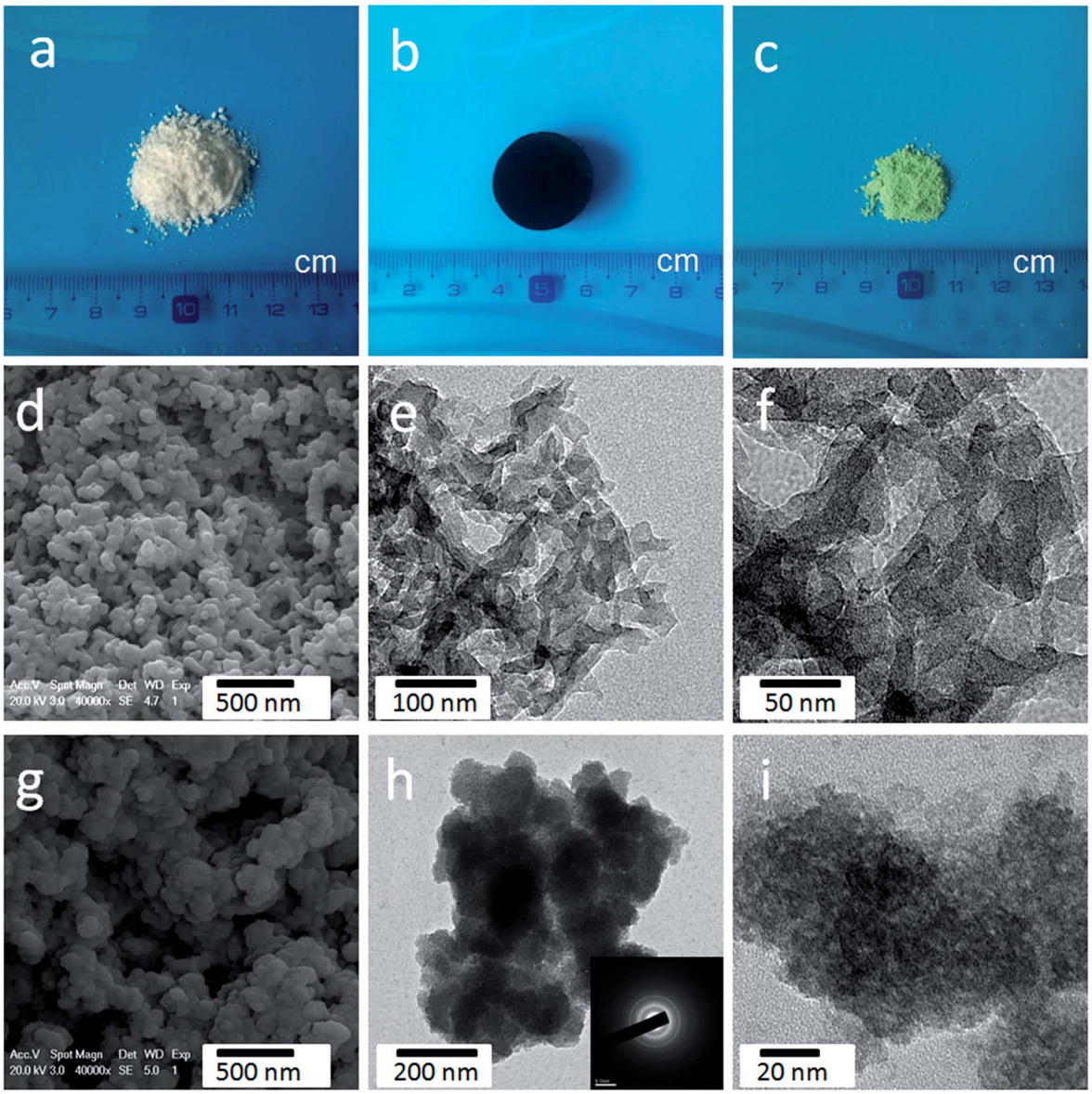

Fig. 2 Photographs of (a) microcrystalline cellulose powder, (b) cellulose-derived CA, and (c) $Ni(OH)_2$. (d) SEM images and (e and f) TEM images of cellulose-derived CA. (g) SEM images and (h and i) TEM images of $Ni(OH)_2$.

of concentric, diffuse rings indicating the polycrystalline structure of the obtained $Ni(OH)_2$ sample.

As shown in the SEM images (Fig. 3a, b, e and f), after the incorporation of $Ni(OH)_2$, the cellulose-derived CA/$Ni(OH)_2$ composite also exhibits the three-dimensional, interconnected, porous nanostructure. From the TEM images (Fig. 3c, d, g and h) we can further see that the morphology of the CA/$Ni(OH)_2$ composite is quite different from those of the cellulose-derived CA and $Ni(OH)_2$. The CA/$Ni(OH)_2$ composite not only keeps the nanoporous structure of the CA but also shows embedded $Ni(OH)_2$ nanoparticles on the interconnected CA backbone. The magnified TEM images (Fig. 3d and h) show that the small $Ni(OH)_2$ nanoparticles in the ranges of 3–8 and 3–10 nm are homogeneously deposited onto the CA backbone for CA/$Ni(OH)_2$/0.30 and CA/$Ni(OH)_2$/0.75, respectively. Apparently, the particle size of $Ni(OH)_2$ in the CA/$Ni(OH)_2$ composite is much smaller than that of the pure $Ni(OH)_2$ sample and there is no large $Ni(OH)_2$ aggregate observed in the composite. This composite nanostructure would enable $Ni(OH)_2$ to be well exposed to the electrolyte and make the charge travel distance within the $Ni(OH)_2$ domain much shorter. The corresponding selected area electron diffraction pattern of CA/$Ni(OH)_2$/0.75 (the inset of Fig. 3h) shows weaker concentric diffuse rings, compared to those of pure $Ni(OH)_2$, which indicates the lower crystallinity of $Ni(OH)_2$ in the CA/$Ni(OH)_2$ composite, compared to that of the pure $Ni(OH)_2$ sample. Fig. 3i and j show the appearance of CA/$Ni(OH)_2$/0.30 and CA/$Ni(OH)_2$/0.75, respectively. It can be seen that the CA/$Ni(OH)_2$ composite maintains the initial shape of the CA and exhibits little shrinkage after the two-step chemical precipitation process.

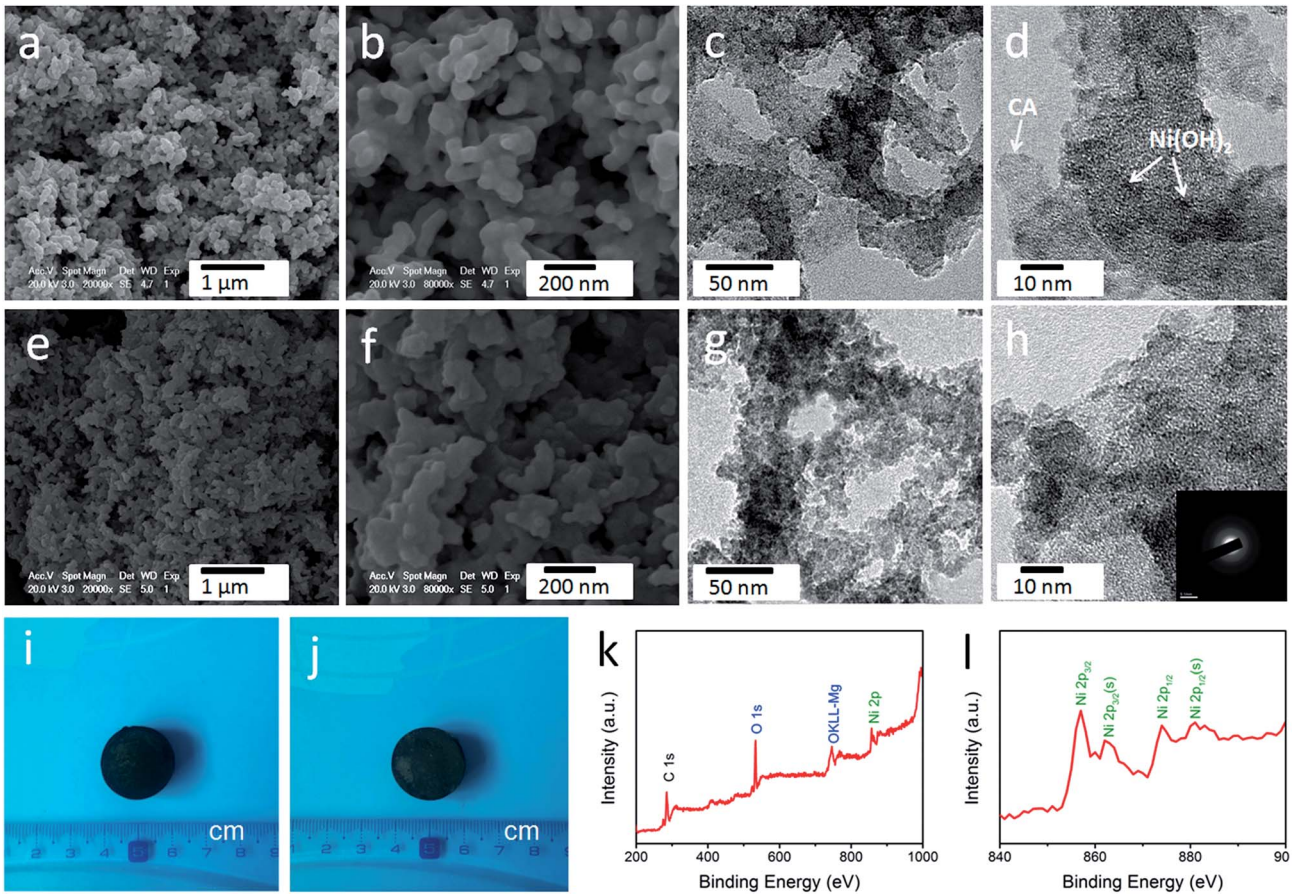

Fig. 3 (a and b) SEM images and (c and d) TEM images of CA/Ni(OH)$_2$/0.30. (e and f) SEM images and (g and h) TEM images of CA/Ni(OH)$_2$/0.75. Photographs of (i) CA/Ni(OH)$_2$/0.30 and (j) CA/Ni(OH)$_2$/0.75. (k) XPS spectra and (l) Ni 2p XPS spectra of CA/Ni(OH)$_2$/0.75. The inset is the selected area electron diffraction pattern of CA/Ni(OH)$_2$/0.75.

3.3 Composition

The composition of CA/Ni(OH)$_2$/0.75 was examined by XPS measurement as shown in Fig. 3k and l. The XPS spectra confirm the presence of C, O, and Ni elements in the CA/Ni(OH)$_2$ composite. It should be noted that the Ni 2p XPS spectra show two major peaks at around 856 and 874 eV, corresponding to Ni 2p$_{3/2}$ and Ni 2p$_{1/2}$, respectively, with a spin-energy separation of approximately 18 eV, which is characteristic of a Ni(OH)$_2$ phase.[47] The satellite peaks at around 862 and 880 eV, corresponding to Ni 2p$_{3/2}$ and Ni 2p$_{1/2}$, respectively, are also observed.

The compositions of the cellulose-derived CA and CA/Ni(OH)$_2$ composite were further investigated by Raman spectra and Fourier transform infrared (FTIR) spectral measurements. Fig. 4a shows the Raman spectra of the CA and CA/Ni(OH)$_2$ composite. All the curves exhibit two broad peaks at around 1361 and 1583 cm^{-1}, corresponding to the D and G bands of the CA. The G band represents the in-plane bond-stretching motion of the pairs of C sp^2 atoms, whereas the D band is assigned to the breathing modes of rings or κ-point phonons of A$_{1g}$ symmetry.[19] Probably due to the incorporation of Ni(OH)$_2$, these two peaks of the CA/Ni(OH)$_2$ composite are apparently weaker than those of the CA. It should be noted that the spectra of the CA/Ni(OH)$_2$ composite exhibits two additional broad peaks at around 361 and 530 cm^{-1}, which can be assigned to the E$_u$(T) and A$_{2u}$(T) lattice vibrations of Ni(OH)$_2$, respectively.[20,48] Due to the higher loading of Ni(OH)$_2$, the peaks at 361 and 530 cm^{-1} of

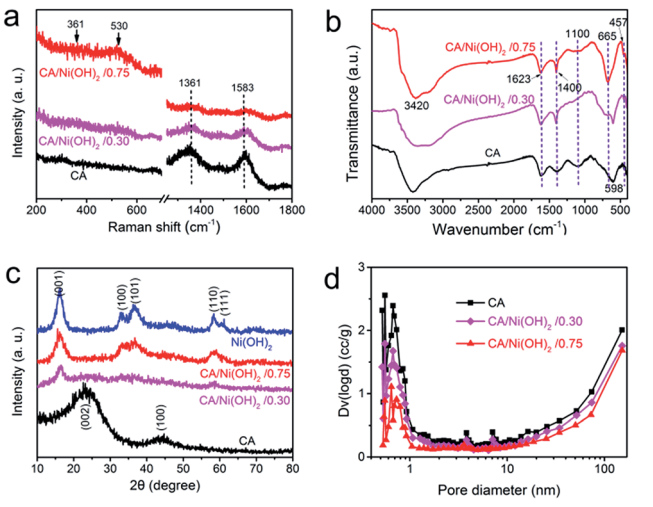

Fig. 4 (a) Raman spectra and (b) FTIR spectra of the cellulose-derived CA and CA/Ni(OH)$_2$ composite. (c) XRD patterns of cellulose-derived CA, Ni(OH)$_2$, and CA/Ni(OH)$_2$ composite. (d) Pore size distributions of cellulose-derived CA and CA/Ni(OH)$_2$ composite.

$CA/Ni(OH)_2$/0.75 are more apparent than those of $CA/Ni(OH)_2$/0.30. The FTIR spectra of the CA and $CA/Ni(OH)_2$ composite are shown in Fig. 4b. The broad band at 3420 cm^{-1} is attributed to the O–H stretching vibration, whereas the band at 1400 cm^{-1} is assigned to the C–H bond.[49] The band at 1623 cm^{-1} can be assigned to H–O–H bending vibration of weakly bound H_2O adsorbed on the nanoparticle surface of aerogels.[50] The band at 1100 cm^{-1} can be ascribed to the C–O–C stretching vibration.[34] These bands indicate that there are –OH, C–H, H_2O, and C–O–C in the CA and the $CA/Ni(OH)_2$ composite. In addition, unlike the spectrum of the CA, the spectrum of the $CA/Ni(OH)_2$ composite shows two bands at around 665 and 457 cm^{-1} that are ascribed to the δ_{OH} and ν_{Ni-OH} vibrations respectively, which become more intense with higher loading of $Ni(OH)_2$.[19]

Fig. 4c shows the XRD patterns of the cellulose-derived CA, $Ni(OH)_2$ and $CA/Ni(OH)_2$ composite. The two broad diffraction peaks at around 24° and 43° in the XRD patterns correspond to the CA.[1,41] The XRD pattern of $Ni(OH)_2$ shows broad peaks at 16.2°, 32.9°, 36.6°, 58.4°, and 61.1°, which are assigned to the (001), (100), (101), (110), and (111) lattice planes of β-$Ni(OH)_2$, respectively (JCPDS no: 14-0117).[16,17] These five broad peaks can also be identified in the diffraction pattern of $CA/Ni(OH)_2$/0.75. Moreover, the peaks at 16.2° and 58.4° can be identified in the diffraction pattern of $CA/Ni(OH)_2$/0.30. These broad peaks indicate the successful incorporation of $Ni(OH)_2$ and the polycrystalline structure of the $CA/Ni(OH)_2$ composite. In addition, the weaker peaks of the $CA/Ni(OH)_2$ composite compared to those of $Ni(OH)_2$ reveal the lower crystallinity of $Ni(OH)_2$ in the $CA/Ni(OH)_2$ composite, compared to that of the pure $Ni(OH)_2$ sample. These results are consistent with the abovementioned selected area electron diffraction pattern (the insets of Fig. 2h and 3h) analysis. The lower crystallinity is probably because the nanoporous CA matrix restrains the growth of large aggregates and enables the homogenous deposition of smaller $Ni(OH)_2$ nanocrystals than those of the $Ni(OH)_2$ sample prepared without the matrix, which was confirmed by the TEM results mentioned above.

3.4 Pore structure and specific surface area

The pore size distributions of the cellulose-derived CA and $CA/Ni(OH)_2$ composite were measured by a N_2 adsorption analyzer using the Brunauer–Emmett–Teller (BET) N_2 adsorption/desorption technique as shown in Fig. 4d. It was observed that both the CA and $CA/Ni(OH)_2$ composite exhibit micropores (<2 nm), mesopores (2–50 nm) and macropores (>50 nm), and show a pore size peak located in the micropore region. The pore volume, particularly the micropore volume, decreased after the incorporation of $Ni(OH)_2$, which further decreased with higher loading of $Ni(OH)_2$. Table 1 details the pore structural parameters of the CA and $CA/Ni(OH)_2$ composite. The specific surface area and total pore volume decreased from 883 $m^2\ g^{-1}$ and 1.74 $cm^3\ g^{-1}$ for the CA to 327 $m^2\ g^{-1}$ and 1.23 $cm^3\ g^{-1}$, respectively for $CA/Ni(OH)_2$/0.75. The corresponding micropore specific surface area and micropore volume were reduced from 506 $m^2\ g^{-1}$ and 0.202 $cm^3\ g^{-1}$ for the CA to 125 $m^2\ g^{-1}$ and 0.054 $cm^3\ g^{-1}$, respectively for $CA/Ni(OH)_2$/0.75. There are probably two main reasons for the decrease in pore volume and specific surface area, particularly micropore volume and micropore specific surface area. On one hand, nanopores in the CA matrix are partially filled with $Ni(OH)_2$ nanoparticles during the precipitation process. On the other hand, some nanopores of the CA may collapse during the ambient drying process. According to the report,[51] the deposition of polymer follows the hierarchical structure of aerogels. Thus, $Ni(OH)_2$ forms a conformal coating around primary particles and then fills secondary particles, followed by accumulating mostly on and around secondary particles. This deposition process results in the significant decrease of micropores in the hierarchically porous CAs. Mainly due to the decrease in micropores, after the incorporation of $Ni(OH)_2$, the mean pore diameter increases from 9.48 nm for the CA to 13.1 nm for $CA/Ni(OH)_2$/0.30 and 15.0 nm for $CA/Ni(OH)_2$/0.75. The N_2 adsorption/desorption isotherms of the cellulose-derived CA and $CA/Ni(OH)_2$/0.75 are additionally provided in Fig. S2.† Both of the aerogels exhibit type IV isotherms and type H3 hysteresis loops, indicating the nanoporous 3D network structure. This high-surface-area, highly porous composite nanostructure would enable active $Ni(OH)_2$ to be well exposed to the electrolyte and enhance the efficiency of the electrolyte ions and electron transport within the electrode material, which could significantly enhance the efficiency of capacity generation from $Ni(OH)_2$.

3.5 Electrochemical performances

The electrochemical performances of the $CA/Ni(OH)_2$ composite as well as the cellulose-derived CA and $Ni(OH)_2$ were investigated using cyclic voltammetric (CV) measurements within the potential window from −0.1 to 0.45 V and −0.3 to 0.6 V in 6 M KOH aqueous solution with a two-electrode system. The CV curves of the CA, $Ni(OH)_2$, and $CA/Ni(OH)_2$ composite at a scan rate of 25 mV s^{-1} are shown in Fig. 5a. It can be seen that

Table 1 The pore structural parameters of cellulose-derived CA and $CA/Ni(OH)_2$ composite

Sample	S_{BET}[a] (S_{mic}[b]) ($m^2\ g^{-1}$)	D[c] (nm)	V_t[d] (V_{mic}[e]) ($cm^3\ g^{-1}$)
Cellulose-derived CA	883 (506)	9.48	1.74 (0.202)
$CA/Ni(OH)_2$/0.30	529 (238)	13.1	1.42 (0.097)
$CA/Ni(OH)_2$/0.75	327 (125)	15.0	1.23 (0.054)

[a] Specific surface area. [b] Micropore specific surface area from *t*-method micropore analysis. [c] Mean pore diameter. [d] Total pore volume. [e] Micropore volume from *t*-method micropore analysis.

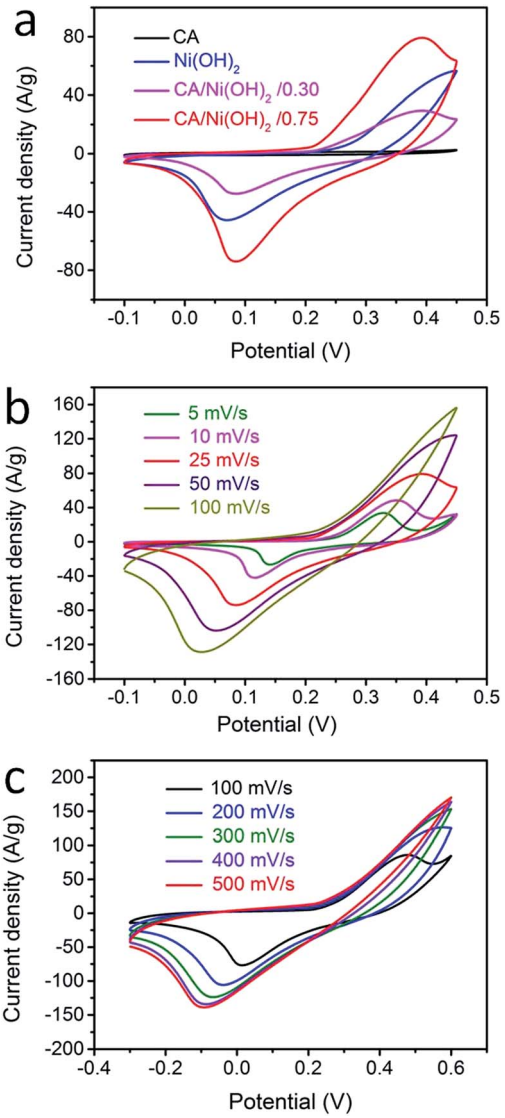

Fig. 5 (a) CV curves of cellulose-derived CA, $Ni(OH)_2$, and CA/$Ni(OH)_2$ composite at a scan rate of 25 mV s^{-1}. (b) CV curves of CA/$Ni(OH)_2$/0.75 at different scan rates ranging from 5 to 100 mV s^{-1}. (c) CV curves of CA/$Ni(OH)_2$/0.75 in a potential window of −0.3 to 0.6 V at scan rates of 100, 200, 300, 400 and 500 mV s^{-1}.

the CV curve area of the CA is much smaller than those of $Ni(OH)_2$ and CA/$Ni(OH)_2$ composite, indicating the negligible capacity of the CA compared to those of $Ni(OH)_2$ and CA/$Ni(OH)_2$ composite. The maximum CV curve area of CA/$Ni(OH)_2$/0.75 indicates the better electrochemical performance of CA/$Ni(OH)_2$/0.75 than those of other samples. It should be noted that the CV curve of the CA/$Ni(OH)_2$ composite shows a pair of oxidation and reduction peaks, which result from the reversible reaction of $Ni(OH)_2 + OH^- \leftrightarrow NiOOH + H_2O + e^-$, involving the intercalation and deintercalation of protons.[2,8] From the CV curves at different scan rates (Fig. 5b) we can see that the oxidation peak of CA/$Ni(OH)_2$/0.75 shifts to a more positive position and the reduction peak shifts to a more negative position with an increase in scan rate. This is probably due to the increase of the internal diffusion resistance within the active material with an increase of scan rate.[52] In addition, the CV curves of the CA at different scan rates are given in Fig. S3.† The CV curves of CA/$Ni(OH)_2$/0.75 in a wide potential window of −0.3 to 0.6 V at scan rates of 100, 200, 300, 400 and 500 mV s^{-1} were also carried out (Fig. 5c). With a further increase in the scan rate, the oxidation and reduction peaks further shift to the positive and negative directions, respectively.

The galvanostatic charge/discharge performances of the CA/$Ni(OH)_2$ composite and $Ni(OH)_2$ were also investigated at current densities ranging from 1 to 20 A g^{-1}, as shown in Fig. 6a and b. The charge/discharge curves of both $Ni(OH)_2$ and CA/$Ni(OH)_2$/0.75 show a significant deviation from the typical triangular shape of electric double layer capacitances, indicating the faradaic redox reaction characteristics of the charge storage. This result is consistent with the abovementioned analysis of CV curves. The specific capacities of CA/$Ni(OH)_2$/0.75 from the discharge curves based on the mass of the active material $Ni(OH)_2$ are calculated to be 1906 and 1206 C g^{-1} at a current density of 1 and 20 A g^{-1}, respectively, approximately 700 F g^{-1} higher than those of $Ni(OH)_2$ (1164 and 540 C g^{-1}, respectively). In addition, the specific capacities of CA/$Ni(OH)_2$/0.75 based on the mass of the entire CA/$Ni(OH)_2$ electrodes (1430 and 904 C g^{-1} at 1 and 20 A g^{-1}, respectively) are also higher than those of $Ni(OH)_2$. Both the samples show decreased specific capacity with increasing current density as shown in Fig. 6c. This is because ion transport within the porous structure lags behind the potential variation, and the internal resistances for charge carriers retard the electrochemical performance of the active materials at higher current densities.[33] However, when the current density is increased from 1 to 20 A g^{-1}, about 63% specific capacity of CA/$Ni(OH)_2$/0.75 is retained, well above that of $Ni(OH)_2$ (46%), indicating a better diffusion of electrolyte ions and electrons of the CA/$Ni(OH)_2$

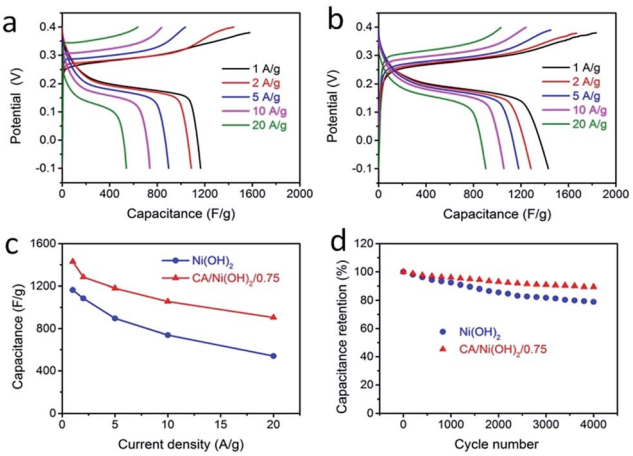

Fig. 6 Galvanostatic charge/discharge curves of (a) $Ni(OH)_2$ and (b) CA/$Ni(OH)_2$/0.75 at different constant current densities, ranging from 1 to 20 A g^{-1}. (c) Specific capacitances at various discharge current densities. Here, the capacitances of CA/$Ni(OH)_2$/0.75 are based on the mass of the entire CA/$Ni(OH)_2$ electrodes. (d) Cycling performance measured at a current density of 20 A g^{-1} in a potential range of −0.1 to 0.4 V.

composite compared to that of $Ni(OH)_2$ at high current densities. The higher specific capacity of CA/$Ni(OH)_2$/0.75 compared to that of $Ni(OH)_2$ is probably attributed to the enhanced efficiency of capacity generation due to the fuller utilization of the well-exposed $Ni(OH)_2$ nanoparticles on the interconnected, three-dimensional, high-surface-area CA matrix. The specific capacity is further compared to that of the reported $Ni(OH)_2$-based materials. The specific capacity of CA/$Ni(OH)_2$/0.75 at a current density of 1 A g^{-1} is lower than that of Ni foam/$Ni(OH)_2$ (2384 F g^{-1}), but higher than that of carbon fiber/$Ni(OH)_2$ (1416 F g^{-1}).[53,54] The specific capacity of CA/$Ni(OH)_2$/0.75 at a current density of 2 A g^{-1} is higher than that of graphene/CNT/$Ni(OH)_2$ (1212 F g^{-1}).[21]

The cycling stabilities of $Ni(OH)_2$ and CA/$Ni(OH)_2$ composite were further investigated at a current density of 20 A g^{-1} as shown in Fig. 6d. After 4000 cycles, the specific capacitance of CA/$Ni(OH)_2$/0.75 maintains 89% of the initial capacitance, higher than that of $Ni(OH)_2$ (79%). This confirms that the cycling stability of $Ni(OH)_2$ is effectively enhanced by introducing the CA as the conductive and nanoporous matrix. The capacitance loss is probably due to the loss of the electrical contact between the porous CA and the active materials, namely $Ni(OH)_2$, resulting from the volume change in the active material during cycling.

The Nyquist plots of the cellulose-derived CA, $Ni(OH)_2$, and CA/$Ni(OH)_2$ composite obtained using AC electrochemical impedance spectroscopy in the frequency range from 0.5 Hz to 0.1 MHz are shown in Fig. S4.† In the low frequency region, the Nyquist plots of CA/$Ni(OH)_2$/0.75 show a more vertical curve compared to that of $Ni(OH)_2$, indicating better capacitive behavior.[21] The equivalent series resistance of the energy storage devices can be obtained from the intercept at the real axis in the Nyquist plot at high frequency[55] and it is composed of the ionic resistance of the electrolytes, electronic resistance of the electrode materials, and interface resistance. The obtained equivalent series resistance of CA/$Ni(OH)_2$/0.75 is 0.69 Ω, which is higher than that of the CA (0.63 Ω) but lower than that of $Ni(OH)_2$ (0.95 Ω). This demonstrates that the internal resistance in the energy storage devices of the CA/$Ni(OH)_2$ composite is smaller than that of $Ni(OH)_2$, indicating better electrochemical performance of the CA/$Ni(OH)_2$ composite compared to that of $Ni(OH)_2$. Considering the renewable carbon source, high specific capacity and good cycling stability, the cellulose-derived CA/$Ni(OH)_2$ composite materials may have application potential in low-cost and high-performance energy storage devices.

4. Conclusion

A wet chemical approach has been applied to the synthesis of nano-architectured carbon aerogel/$Ni(OH)_2$ composites, which combines the sol–gel preparation of highly porous carbon aerogel using microcrystalline cellulose as the carbon source and the subsequent homogeneous deposition of $Ni(OH)_2$ nanoparticles onto the backbone of the obtained carbon aerogel *via* a two-step chemical precipitation process. The deposited $Ni(OH)_2$ on the carbon aerogel shows much smaller size and more uniform dispersion, compared to the $Ni(OH)_2$ prepared by a conventional method. The specific capacitance of the resulting composite was 1906 and 1206 F g^{-1} at a current density of 1 and 20 A g^{-1} respectively, much higher than that of $Ni(OH)_2$. The composite also showed good cycling stability with 89% of the capacitance retention after 4000 cycles. The good electrochemical performance is attributed to the enhanced efficiency of capacitance generation from $Ni(OH)_2$ due to the better utilization of the well-exposed $Ni(OH)_2$ nanoparticles on the interconnected, three-dimensional, high-surface-area carbon aerogel matrix. The cellulose-derived carbon aerogel/$Ni(OH)_2$ composite materials may have application potentials in low-cost and high-performance energy storage devices.

Acknowledgements

We thank the financial support from the National Natural Science Foundation of China (No. U1230113), National key Technology R&D Program of China (No. 2013BAJ01B01), National High Technology Research and Development Program of China (863) (No. 2013AA031801), Shanghai Aerospace Science and Technology Innovation Fund (No. SAST201469) and Project Funded by China Postdoctoral Science Foundation (No. 0800229072).

Notes and references

1 H.-C. Chien, W.-Y. Cheng, Y.-H. Wang and S.-Y. Lu, *Adv. Funct. Mater.*, 2012, **22**, 5038–5043.
2 J. Ji, L. L. Zhang, H. Ji, Y. Li, X. Zhao, X. Bai, X. Fan, F. Zhang and R. S. Ruoff, *ACS Nano*, 2013, **7**, 6237–6243.
3 C.-C. Hu, K.-H. Chang, M.-C. Lin and Y.-T. Wu, *Nano Lett.*, 2006, **6**, 2690–2695.
4 Z. S. Wu, W. C. Ren, D. W. Wang, F. Li, B. L. Liu and H. M. Cheng, *ACS Nano*, 2010, **4**, 5835–5842.
5 T.-Y. Wei, C.-H. Chen, K.-H. Chang, S.-Y. Lu and C.-C. Hu, *Chem. Mater.*, 2009, **21**, 3228–3233.
6 J.-W. Lang, L.-B. Kong, W.-J. Wu, Y.-C. Luo and L. Kang, *Chem. Commun.*, 2008, **44**, 4213–4215.
7 Y. Yang, L. Li, G. Ruan, H. Fei, C. Xiang, X. Fan and J. M. Tour, *ACS Nano*, 2014, **8**, 9622–9628.
8 Z. Tang, C. Tang and H. Gong, *Adv. Funct. Mater.*, 2012, **22**, 1272–1278.
9 H. Wang, H. S. Casalongue, Y. Liang and H. Dai, *J. Am. Chem. Soc.*, 2010, **132**, 7472–7477.
10 G. Wang, L. Zhang and J. Zhang, *Chem. Soc. Rev.*, 2012, **41**, 797–828.
11 J. Li, F. Luo, X. Tian, Y. Lei, H. Yuan and D. Xiao, *J. Power Sources*, 2013, **243**, 721–727.
12 J. H. Park, O. O. Park, K. H. Shin, C. S. Jin and J. H. Kim, *Electrochem. Solid-State Lett.*, 2002, **5**, H7–H10.
13 Q. Huang, X. Wang, J. Li, C. Dai, S. Gamboa and P. J. Sebastian, *J. Power Sources*, 2007, **164**, 425–429.
14 G. Hasegawa, T. Deguchi, K. Kanamori, Y. Kobayashi, H. Kageyama, T. Abe and K. Nakanishi, *Chem. Mater.*, 2015, **27**, 4703–4712.
15 R. R. Salunkhe, J. Lin, V. Malgras, S. X. Dou, J. H. Kim and Y. Yamauchi, *Nano Energy*, 2015, **11**, 211–218.

16 D. P. Dubal, G. S. Gund, C. D. Lokhande and R. Holze, *ACS Appl. Mater. Interfaces*, 2013, **5**, 2446–2454.
17 M. Shahid, J. Liu, I. Shakir, M. F. Warsi, M. Nadeem and Y. Kwon, *Electrochim. Acta*, 2012, **85**, 243–247.
18 X. Ma, J. Liu, C. Liang, X. Gong and R. Che, *J. Mater. Chem. A*, 2014, **2**, 12692–12696.
19 J. Yan, Z. Fan, W. Sun, G. Ning, T. Wei, Q. Zhang, R. Zhang, L. Zhi and F. Wei, *Adv. Funct. Mater.*, 2012, **22**, 2632–2641.
20 J. Yan, W. Sun, T. Wei, Q. Zhang, Z. Fan and F. Wei, *J. Mater. Chem.*, 2012, **22**, 11494–11502.
21 Y. Xu, X. Huang, Z. Lin, X. Zhong, Y. Huang and X. Duan, *Nano Res.*, 2013, **6**, 65–76.
22 D. Fang, Z. Chen, X. Liu, Z. Wu and C. Zheng, *Electrochim. Acta*, 2012, **81**, 321–329.
23 J. Xie, X. Sun, N. Zhang, K. Xu, M. Zhou and Y. Xie, *Nano Energy*, 2013, **2**, 65–74.
24 X. H. Xia, D. L. Chao, Z. X. Fan, C. Guan, X. H. Cao, H. Zhang and H. J. Fan, *Nano Lett.*, 2014, **14**, 1651–1658.
25 J. Zhu, Z. Xu and B. N. Lu, *Nano Energy*, 2014, **7**, 114–123.
26 Y. H. Li, Z. Y. Wang and Y. F. Zhang, *J. Alloys Compd.*, 2015, **644**(644), 47–53.
27 D. Shi, L. Zhang, X. Yin, T. J. Huang and H. Gong, *J. Mater. Chem. A*, 2016, **4**, 12144–12151.
28 M. Xie, S. Duan, Y. Shen, K. Fang, Y. Wang, M. Lin and X. Guo, *ACS Energy Lett.*, 2016, **1**, 814–819.
29 P. Xu, C. Miao, K. Cheng, K. Ye, J. Yin, D. Cao, G. Wang and X. Zhang, *Electrochim. Acta*, 2016, **216**, 499–509.
30 R. Wang, A. Jayakumar, C. Xu and J.-M. Lee, *ACS Sustainable Chem. Eng.*, 2016, **4**, 3736–3742.
31 J. Biener, M. Stadermann, M. Suss, M. A. Worsley, M. M. Biener, K. A. Rose and T. F. Baumann, *Energy Environ. Sci.*, 2011, **4**, 656–667.
32 X. Wu and A. Xu, *J. Mater. Chem. A*, 2014, **2**, 4852–4864.
33 Y.-H. Lin, T.-Y. Wei, H.-C. Chien and S.-Y. Lu, *Adv. Energy Mater.*, 2011, **1**, 901–907.
34 X. Wu, T. Wen, H. Guo, S. Yang, X. Wang and A. Xu, *ACS Nano*, 2013, **7**, 3589–3597.
35 Y. J. Lee, J. C. Jung, J. Yi, S. H. Baeck, J. R. Yoon and I. K. Song, *Curr. Appl. Phys.*, 2010, **10**, 682–686.
36 R. W. Pekala, J. C. Farmer, C. T. Alviso, T. D. Tram, S. T. Mayer, J. M. Miller and B. Dunn, *J. Non-Cryst. Solids*, 1998, **225**, 74–80.
37 Y. Zhu, H. Hu, W. C. Li and X. Zhang, *J. Power Sources*, 2006, **162**, 738–742.
38 C. Moreno-Castilla, M. B. Dawidziuk, F. Carrasco-Marin and Z. Zapata-Bennabithe, *Carbon*, 2011, **49**, 3808–3819.
39 Z. Y. Wu, C. Li, H. W. Liang, J. F. Chen and S. H. Yu, *Angew. Chem.*, 2013, **125**, 2997–3001.
40 A. G. Sadekar, S. S. Mahadik, A. N. Bang, Z. J. Larimore, C. A. Wisner, M. F. Bertino, A. K. Kalkan, J. T. Mang, C. Sotiriou-Leventis and N. Leventis, *Chem. Mater.*, 2012, **24**, 26–47.
41 L. Wang, C. Schutz, G. Salazar-Alvarez and M. M. Titirici, *RSC Adv.*, 2014, **4**, 17549–17554.
42 E. Guilminot, F. Fischer, M. Chatenet, A. Rigacci, S. Berthon-Fabry, P. Achard and E. Chainet, *J. Power Sources*, 2007, **166**, 104–111.
43 B. Grzyb, C. Hildenbrand, S. Berthon-Fabry, D. Begin, N. Job, A. Rigacci and P. Achard, *Carbon*, 2010, **48**, 2297–2307.
44 K. Gao, Z. Shao, X. Wang, Y. Zhang, W. Wang and F. Wang, *RSC Adv.*, 2013, **3**, 15058–15064.
45 Z. Y. Wu, H. W. Liang, C. Li, B. C. Hu, X. X. Xu, Q. Wang, J. Chen and S. Yu, *Nano Res.*, 2014, **7**, 1861–1872.
46 G. Zu, J. Shen, L. Zou, F. Wang, X. Wang, Y. Zhang and X. Yao, *Carbon*, 2016, **99**, 203–211.
47 S. Bag and C. R. Raj, *J. Mater. Chem. A*, 2014, **2**, 17848–17856.
48 S. R. Shieh and T. S. Duffy, *Phys. Rev. B: Condens. Matter Mater. Phys.*, 2002, **66**, 134301–134308.
49 G. Zu, J. Shen, W. Wang, L. Zou, Y. Lian and Z. Zhang, *ACS Appl. Mater. Interfaces*, 2015, **7**, 5400–5409.
50 G. S. Li, L. P. Li, J. Boerio-Goates and B. F. Woodfield, *J. Am. Chem. Soc.*, 2005, **127**, 8659–8666.
51 D. P. Mohite, Z. J. Larimore, H. Lu, J. T. Mang, C. Sotiriou-Leventis and N. Leventis, *Chem. Mater.*, 2012, **24**, 3434–3448.
52 U. M. Patil, K. V. Gurav, V. J. Fulari, C. D. Lokhande and O. S. Joo, *J. Power Sources*, 2009, **188**, 338–342.
53 X. Xiong, D. Ding, D. Chen, G. Waller, Y. Bu, Z. Wang and M. Liu, *Nano Energy*, 2015, **11**, 154–161.
54 N. A. Alhebshi, R. B. Rakhi and H. N. Alshareef, *J. Mater. Chem. A*, 2013, **1**, 14897–14903.
55 J. W. Lang, X. B. Yan, X. Y. Yuan, J. Yang and Q. J. Xue, *J. Power Sources*, 2011, **196**, 10472–10478.